Performance of a flying cross bar to incapacitate a long-rod penetrator based on a finite element model

Yo-Han Yoo, Seung Hoon Paik, Jong-Bong Kim & Hyunho Shin

Engineering with Computers
An International Journal for Simulation-Based Engineering

ISSN 0177-0667
Volume 29
Number 4

Engineering with Computers (2013)
29:409-415
DOI 10.1007/s00366-012-0257-y

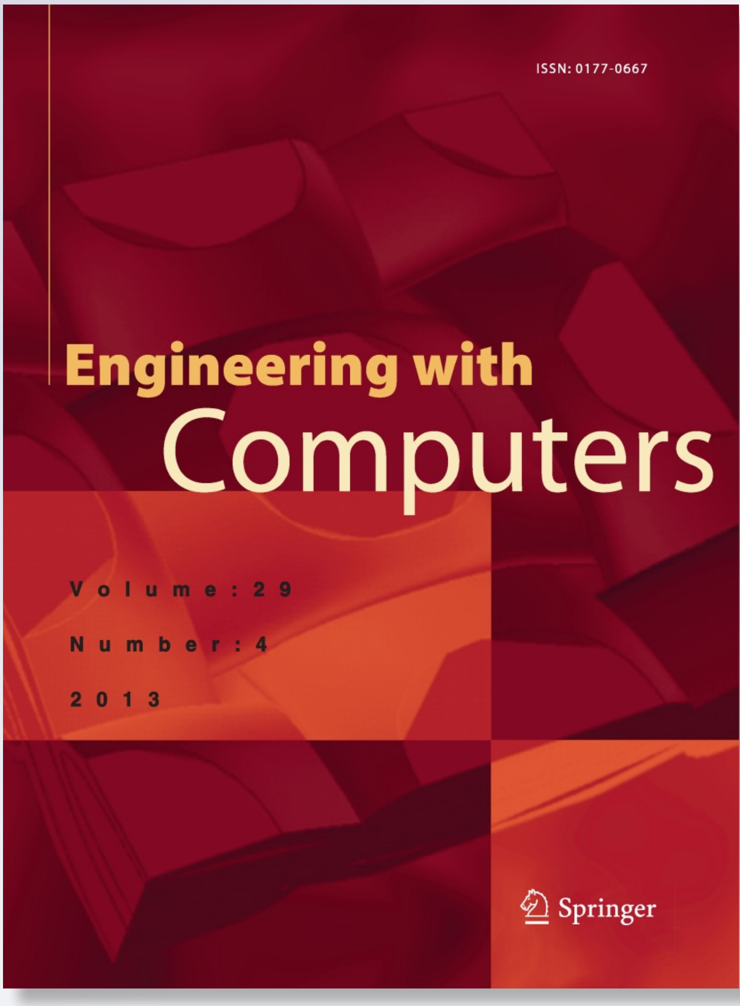

Springer

Engineering with Computers (2013) 29:409–415
DOI 10.1007/s00366-012-0257-y

ORIGINAL ARTICLE

Performance of a flying cross bar to incapacitate a long-rod penetrator based on a finite element model

Yo-Han Yoo · Seung Hoon Paik · Jong-Bong Kim · Hyunho Shin

Received: 21 August 2011 / Accepted: 17 January 2012 / Published online: 2 February 2012

Abstract Performance of a flying cross bar, instead of the flying plate, to incapacitate the long-rod penetrator, has been evaluated numerically based on a finite element model. The length to diameter ratio, *L*/*D*, of the penetrator was 30 and the velocity was 2.0 km/s. The length of the cross bar was fixed to 0.5*L* and the velocity of the bar was determined from its mass and given kinetic energy. The bar was assumed to impact the mid point of the penetrator at 45° of obliquity. The efficiency of flying cross bar is maximum when the diameter of the bar is in the range between 1D and 4D depending on the energy of the bar and the distance to witness block. The protection capability of the bar has been discussed in terms of the shape and lateral displacement of the disturbed penetrator by the flying cross bar.

Y.-H. Yoo
Technology Development Centre, Agency for Defence Development, P.O. Box 35-1, Yuseong, Daejeon 305-600, Republic of Korea

S. H. Paik
Korea Institute of Construction Technology, Goyang, Gyeonggi-do 411-712, Republic of Korea

J.-B. Kim
Department of Automotive Engineering, Seoul National University of Science and Technology, Sungbuk-gu 139-743, Republic of Korea

H. Shin (✉)
Department of Materials Engineering, Gangneung-Wonju National University, Gangneung, Gangwong-do 210-702, Republic of Korea
e-mail: hshin@gwnu.ac.kr

Keywords Flying cross bar · Long-rod penetrator · Active armour · Lateral disturbance

1 Introduction

As a method to protect a long-rod penetrator, single or dual flying plates are usually considered in active armour technology [1–7]. The flying plate is known to transfer lateral loads to the penetrator, which yields deflection, rotation, direction change, and breakage of the penetrator before reaching the main target behind the flying plate. Despite its known efficiency, flying a plate is never a simple task due to the excessive energy taken to fly the plate toward the incoming penetrator [8–10].

A flying cross bar, instead of a flying plate, has been recently considered, and its feasibility to incapacitate the long-rod penetrator has been reported by Liden et al. [11]. Employment of the flying cross bar is believed to be an efficient way to reduce the amount of energy required to fly an object. Provided its protection capability is proven, despite of its very light weight, the problem that has been long overdue is solved to fly it with a greatly reduced amount of energy. In order to exploit the performance of the flying cross bar for the design of a sensor-activated armour, examining the influence of the parameters such as the diameter and kinetic energy (velocity) of the bar on the performance to incapacitate the incoming penetrator is of importance. In this regard, the interaction characteristics of the flying cross bar with the long-rod projectile has been numerically investigated in the current work from the viewpoints of the required kinetic energy of the flying bar and the resultant depth of penetration in a witness block. It will be demonstrated that, at a given kinetic energy, the flying cross bar is strongly superior to the flying plate in defeating a long-rod penetrator.

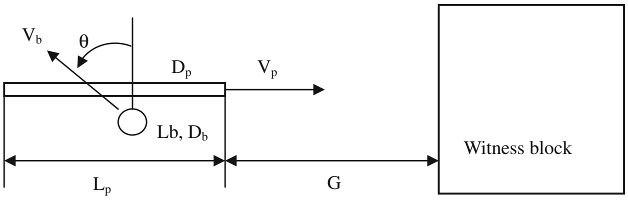

Fig. 1 Schematic cross-sectional view of the model

Table 1 Velocity of bar (in m/s unit), V_b, at a given conditions of KE_b/KE_p and bar diameter (D_b)

KE_b/KE_p	1/128	1/64	1/32	1/16	1/8
$D_b = 1D_p$	373.9	528.7	747.7	1057.4	1495.4
$D_b = 1.5D_p$	249.2	352.5	498.5	705.0	997.0
$D_b = 2D_p$	186.9	264.4	373.9	528.7	747.7
$D_b = 3D_p$	124.6	176.2	249.2	352.5	498.5
$D_b = 4D_p$	93.5	132.2	186.9	264.4	373.9
$D_b = 5D_p$	74.8	105.7	149.5	211.5	299.1
$D_b = 6D_p$	62.3	88.1	124.6	176.2	249.2
$D_b = 7D_p$	53.4	75.5	106.8	151.1	213.6
$D_b = 8D_p$	46.7	66.1	93.5	132.2	186.9
$D_b = 9D_p$	23.4	33.0	46.7	66.1	93.5

2 Numerical analysis

Figure 1 shows the schematic cross-sectional view of the model. The length (L_p) and the diameter (D_p) of the penetrator were 150 and 5 mm, respectively ($L_p/D_p = 30$). The velocity of penetrator (V_p) was fixed to 2 km/s, and thus the kinetic energy of the penetrator (tungsten heavy alloy), KE_p, was fixed to 1.037×10^5 J. An increased length of cross bar L_b would increase the probability of impact while increasing the mass. The length of flying cross bar (L_b) was selected as $0.5L_p$ ($L_b = 75$ mm) in the present study. As the energy required to drive the cross bar is an important issue, the kinetic energy of the cross bar (KE_b) was varied with reference to KE_p: $KE_b/KE_p = 1/128$, 1/64, 1/32, 1/16, 1/8. At each aimed KE_b value, the diameter of the cross bar (D_b) was varied independently: $D_b/D_p = 1$, 1.5, 2, 3, 4, 5, 6, 7, 8, 16, where D_p is the diameter of the penetrator. An increased D_b yields decreased bar velocity at a given KE_b, as the length of the bar has been fixed. The velocity of the bar at given conditions of KE_b/KE_p and bar diameter (D_b) is shown in Table 1. The cross bar was assumed to impact the middle of the penetrator at 45° of obliquity ($\theta = 45^o$).[1] The witness block was 200 mm in height, 50 mm in width, and 250 mm in length.

[1] Hitting the midpoint of the penetrator would be rare in practical situation; The cases of hitting other points will be the subject of a future work.

The protection effectiveness generally increases as the distance to witness block from the location of impact increases since the residual penetrator may rotate, move laterally, and/or deform more as the flight time increases after it is disturbed by the cross bar. Thus, the distance to the witness block (G) is also an important design parameter, which has been varied as, $2L_p$, $3L_p$, and $4L_p$, in this study.

In order to consider strain-rate hardening as well as thermal softening in addition to the strain hardening considered in static deformation of metallic material, Johnson–Cook flow stress model [12] was used,

$$\sigma = (A + B\varepsilon^n)\left(1 + C\ln\frac{\dot{\varepsilon}}{\dot{\varepsilon}_0}\right)\left[1 - \left(\frac{T - T_{\mathrm{ref}}}{T_{\mathrm{melt}} - T_{\mathrm{ref}}}\right)^m\right] \quad (1)$$

Here, σ is flow stress, A the static yield strength, B the strain hardening parameter, ε the equivalent plastic strain, n the strain hardening exponent, C the strain rate parameter, $\dot{\varepsilon}$ the equivalent plastic strain rate, $\dot{\varepsilon}_o$ the reference strain rate, T the temperature, T_{ref} the reference temperature, T_{melt} the melting temperature and m the temperature exponent. The material of the penetrator is tungsten heavy alloy (DX2HCMF), while the cross bar and witness block are high hardness steel (SIS 2541-03), which properties are shown in Table 2 [13].

The equation of state (EOS) used herein is the polynomial model,

$$P = C_0 + C_1\mu + C_2\mu^2 + C_3\mu^3 + (C_4 + C_5\mu + C_6\mu^2)E \quad (2)$$

where, P is pressure and C_i are the coefficients. $\mu = \rho/\rho_0 - 1$ and ρ/ρ_0 is the ratio of density to initial density. E is the internal energy per unit volume. The value C_1 used in this study has been 295 GPa for DX2HCMF and 167 GPa for SIS 2541-3. All other C_i parameters have been set to zero. C_1 is, by itself, the elastic bulk modulus. Thus, the EOS has been reduced to the simplest form, $P = C_1\mu$.

No fracture models were considered for both the penetrator and the bar, and thus any failure of the material by the current simulation is purely caused by the element erosion. As the tensile fracture with crack propagation is not replicated in the present work, actual performance could be different from the predicted results herein. Despite of this limitation, the current numerical results may be used to examine the sensitivity of performance to design parameters, and in general, the trends, rather than absolute values, will probably be correct.

Material erosion has been simulated by eliminating appropriate elements from the model during calculation when they reach a certain plastic strain limit. The empirical equivalent plastic strain limit of 1.5 is adopted in the current work based on a preliminary effort. The validity of the used strain limit together with adopting no fracture models will be checked in this section.

Table 2 Material constants for the Johnson–Cook model [8]

Material	Density (kg/m^3)	A (GPa)	B (GPa)	n	C	m	T_{ref} (K)	T_{melt} (K)
SIS2541-03	7,870	0.75	1.15	0.49	0.014	1.0	293	1,700
DX2HCMF	17,600	1.05	0.177	0.12	0.0275	1.0	293	1,723

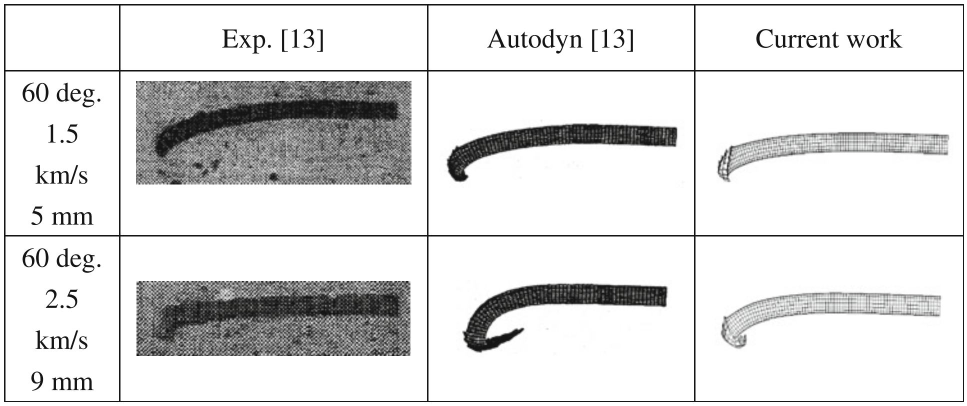

Fig. 2 Comparison of the deformed shapes of the residual penetrator between the current work and existing experimental/numerical results in Ref. [13]

Table 3 Comparison of simulated length and velocity of residual penetrator with existing experiment in Ref. [13]

Oblique angle (°)	V_o (km/s)	Plate thickness (mm)	Residual length (L/L_o)			Residual velocity (V/V_o)		
			Exp. [13]	Numerical [13]	Current work	Exp. [13]	Numerical [13]	Current work
60	1.5	5.0	0.85	0.87	0.84	0.97	0.98	0.97
	2.5	9.0	0.76	0.75	0.75	0.99	0.99	0.98

Only half of the three dimensional space was analyzed considering the symmetry of the model. In order to maintain a similar mesh size of the penetrator to the cross bar and witness block, a fine mesh with the size of 0.67 mm (as compared to $D_p = 5$ mm) was modelled around the impact region of the witness block. Therefore, the total number of elements differed according to the size of the fine mesh region of the block, from ~200,000 to 300,000. A commercial finite element package, LS-DYNA [14], was used for the analysis. The basic element formulation, stress update method, time integration method, and contact-impact algorithm, etc., employed in the package, are described in Ref. [14].

Admitting the limitation of the current simulation in accounting for the tensile fracture mode with crack propagation, the generality (validity) of the current simulation itself was checked *first* by using two cases. The first case was the penetrator that was not fractured after impacting onto an oblique (60°) steel plate in an experiment [13]. The result of our simulation is shown in Fig. 2. Residual lengths and velocities of the penetrator are shown in Table 3. The diameter (D) and length (L) of the penetrator were 5 and 75 mm, respectively, resulting in an L/D ratio of 15. The thicknesses of the plate were 5 mm when the velocity of the penetrator was 1.5 km/s and 9 mm when 2.5 km/s. The material behaviour was modelled using the Johnson–Cook viscoplastic model. The plate and the penetrator were the same materials as the current work (SIS 2541-03 and DX2HCMF, respectively). Based on Fig. 2 and Table 3,[2] the current simulation shows good agreement with the experimental data as well as the numerical analysis shown in Ref. [13].

The second case was the penetration event in the witness block, that does not involve the failure mode such as the crack-involved tensile fracture. The simulated depth of penetration P_o in the witness block by the undisturbed penetrator was compared with the existing values in the literature. P_o was 183.6 mm at the impact velocity of 2.0 km/s in our separate simulation, while it was 182.9 mm (Eq. 5 in Ref. [15]) or 176.1 mm (Eq. 12 in Ref. [16]) in the literature. The material of the penetrator in Refs. [15, 16] was a tungsten alloy; however, it was not exactly the same grade as that used in this study. Furthermore, P_o in Ref. [15] was the extrapolated value from approximate equation to the experiment up to 1.8 km/s of the penetrator velocity, while Ref. [16] was based on the approximate

[2] In Table 3, the decrease of velocity after the impact is so small; The velocity ratio (V/V_o) of 0.97~0.99 may be within the margin of errors.

equation to the simulation (by CTH code) from 1.5 to 4.5 km/s. Thus, the reliability of the simulation of the penetration process itself is ensured. However, the depth of penetration by the *deformed* penetrator after the interaction with the cross bar has a meaning on a comparative basis between the simulation cases because of the lack of the tensile-crack-involved fracture mode of the penetrator as mentioned before.

3 Results and discussion

Figure 3 shows the effects of KE_b/KE_p, D_b/D_p and G on the normalized depth of penetration in witness block, P/P_o, by the disturbed residual penetrator. P_o is 183.6 mm as described previously. First of all, in all of the diagrams in Fig. 3, the protection efficiency, P/P_o, itself is superior (lower value) as the normalized kinetic energy of the cross bar KE_b/KE_p, increases, regardless of the normalized diameter of the bar, D_b/D_p, and distance to the witness block, G. As D_b/D_p increases, P/P_o initially decreases rapidly, but increases back after a minimum P/P_o. The D_b/D_p yielding minimum P/P_o generally shifts from 1.5 to 4.0 as the kinetic energy of the bar KE_b/KE_p increases. Interestingly, as the kinetic energy of the bar KE_b/KE_p grows larger, the relatively wider range of D_b/D_p shows the smaller depth of penetration. As for the influence of G, the overall trend of P/P_o in terms of D_b/D_p for varying KE_b/KE_p is maintained in a similar fashion. However, the P/P_o at a given condition decreases significantly with G since the penetrator deforms and rotates more as the flying time increases after the impact with the cross bar.

Based on the design parameters shown above, the best protection performance of the flying cross bar is realized when $G = 4L_p$, $D_b/D_p = 4$, and $KE_b/KE_p = 1/8$. In this case, P/P_o is nearly 0.2, which means that flying cross bar incapacitates the penetrator $\sim$80%. To compare this case with the flying plate, the P/P_o was simulated separately using a flying plate with the same kinetic energy that was $KE_{plate}/KE_p = 1/8$, $G = 4L_p$, and $\theta = 45^o$. While there are several choices in the plate thickness and size, the thickness of plate was assumed to be same as the penetrator diameter and the ratio of length and width of the plate was assumed to be 2:1. In simulation, when the penetrator perforated the plate, the residual depth of penetration in the witness block, P/P_o, was 0.45. Purely based on the simulation results herein, the flying cross bar seems to be more efficient than the flying plate at a given kinetic energy. However, care has to be taken to interpret this result; Because flying cross *bar* generally just changes shape of the long-rod penetrator while the long-rod penetrator perforates the *plate*, the simulation results can be drastically different depending on the material and fracture models

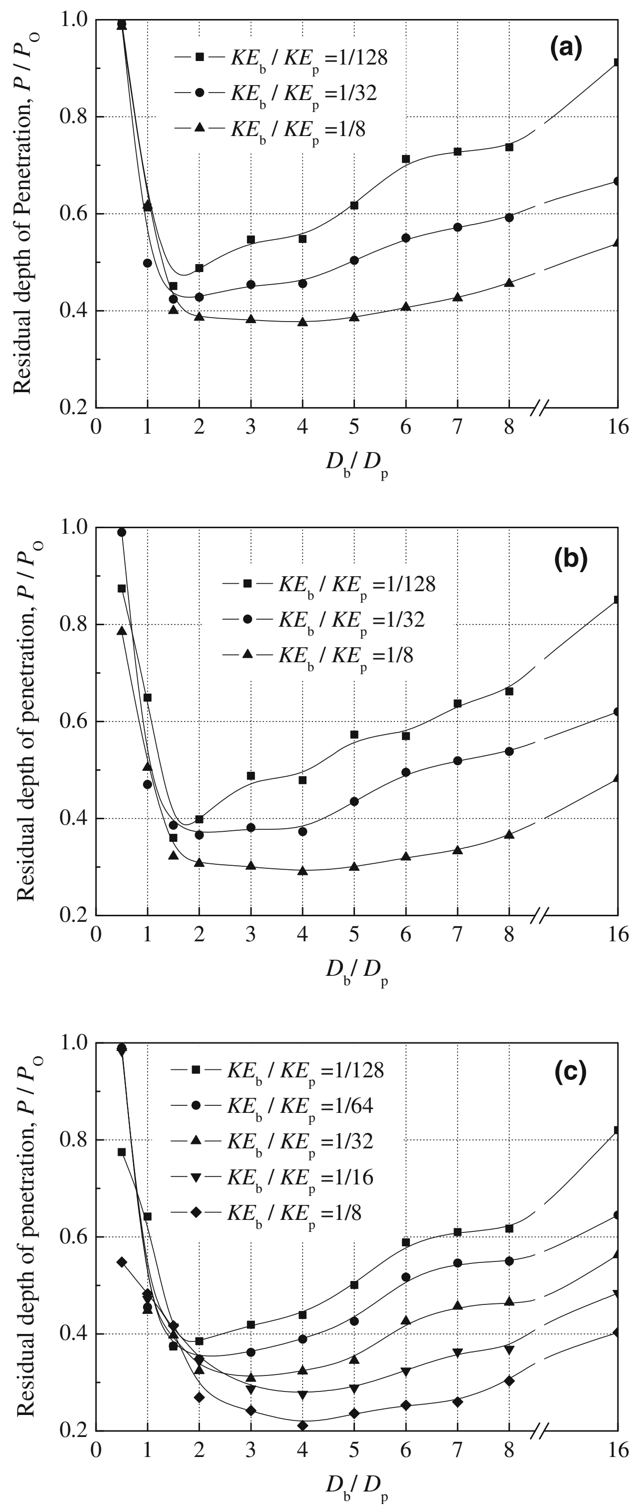

Fig. 3 Change in depth of penetration as a function of bar diameter D_b normalized to the diameter of penetrator D_p. The distances to the witness block G are **a** $2L_p$, **b** $3L_p$, and **c** $4L_p$

adopted in the simulation and the hitting points of the penetrator.

In some impact conditions with the cross bar, the penetrator is broken with somewhat sharp fracture surfaces

[11], which is possibly due to the tensile fracture with crack propagation. Although the current simulation could not account for such fracture mode, nevertheless, the deformed shapes of the penetrator are presented in Figs. 4, 5 for qualitative understanding of the interaction between the bar and the penetrator. Figure 4 shows the deformed penetrator at varying time lapse after the impact for the case of $G = 4L_p$, $KE_b/KE_p = 1/32$, and $D_b/D_p = 2$. Since the flying cross bar impacts the mid point of the penetrator at 45°, the tail portion of the penetrator deflects upward and the magnitude of deflection increases as time lapses. 300 μs is the time just before the penetrator impacts the witness block. In Fig. 5, the deformed shapes of the penetrator are now shown for varying bar diameter D_b/D_p at 300 μs after the impact. The shapes of residual penetrators are distinguished by three patterns. The shape takes the form of a 'hat' when $D_b/D_p = 1$, a reverse-'S' when $D_b/D_p = 2$, and 'L' when $D_b/D_p = 3$ or higher. The magnitude of the lateral displacement of the tail part of the penetrator becomes the largest when $D_b/D_p = 4$ and decreases thereafter. The decrease of the lateral displacement after $D_b/D_p = 4$ is due to the decreased bar velocity associated with increased diameter (mass). Thus, the lateral load was insufficient to deform the penetrator in the lateral direction at the given KE_b/KE_p of 1/32.

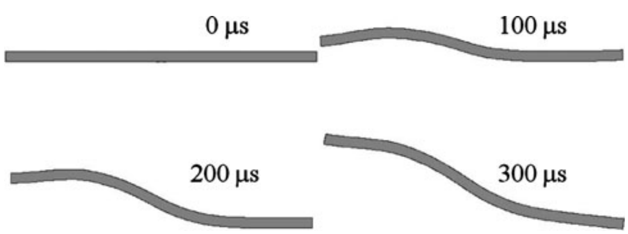

Fig. 4 Deformed shapes of the residual penetrator at varying time after the impact ($G = 4L_p$, $KE_b/KE_p = 1/32$, $D_b/D_p = 2$)

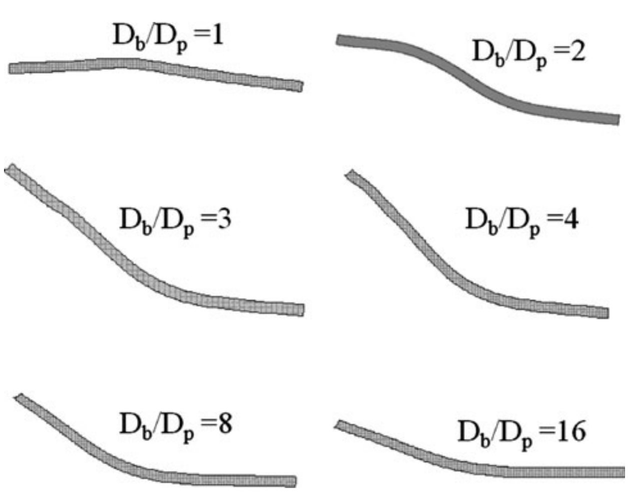

Fig. 5 Deformed shapes of the residual penetrator at 300 μs after the impact for varying D_b/D_p ratio ($G = 4L_p$, $KE_b/KE_p = 1/32$)

The different deformation shapes of the penetrator yield the respective characteristic crater shapes as well as seen in Fig. 6. When $D_b/D_p = 1$, the initial penetration hole develops to two similar ones as penetration progresses. In the cases of $D_b/D_p = 2$ and 3, the shapes of the penetration hall take the forms of 'C' and 'L', respectively. The depth of penetrator is at its minimum at $D_b/D_p = 3$, and increases thereafter. When the cross bar is efficient in disturbing the penetrator (when minimum P/P_o was achieved), the shape of the penetrator takes a form of reverse-'S' (Fig. 5). The same patterns are observed although G and KE_b/KE_p ratio vary (not shown).

After correlating the shape of the residual penetrator and crater shape in the witness block to the minimum depth of penetration, now the correlation between the magnitude of the lateral displacement of the penetrator (based on the movement of the centre of mass) and the depth of penetration is pursued. If the penetrator receives a lateral load during its flight, its flight path deviates from the original one and the degree of deviation, i.e., the magnitude of lateral displacement, accumulates until the residual penetrator reaches the witness block. The total magnitude of the lateral displacement of the penetrator by the time it reaches the witness block located at $G = 4L_p$ has been monitored and the result is shown in Fig. 7 as a function of the bar diameter, D_b/D_p for varying KE_b/KE_p. The ordinate is normalized to the longitudinal displacement (translation distance $4L_p = 600$ mm) for all the cases. The lateral

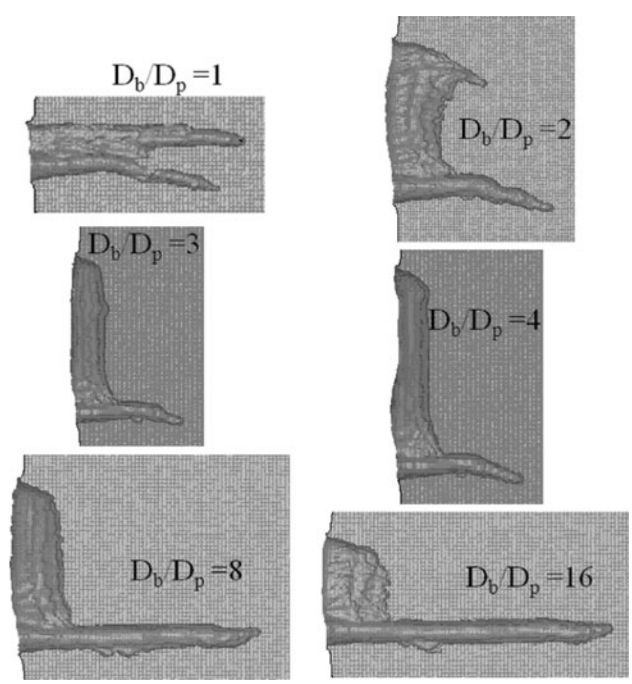

Fig. 6 Shapes of the penetration crater at 500 μs after the impact for varying D_b/D_p ratio ($G = 4L_p$, $KE_b/KE_p = 1/32$). The scales of the sub-figures are the same

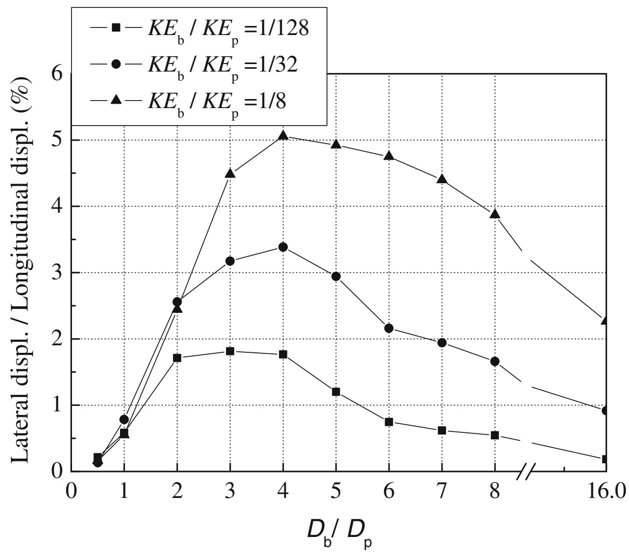

Fig. 7 Normalized lateral displacement of the penetrator as a function of bar diameter D_b normalized to the diameter of penetrator D_p. The distance to the witness block G is $4L_p$

displacement is a rigid body displacement including rotation or averaged displacement. In comparison with the behavior of P/P_o shown in Fig. 3, the roughly parabolic nature is maintained in Fig. 7 as well. Recall that in Fig. 3, the D_b/D_p resulting in minimum P/P_o generally shifted from 1.5 to 4.0 as KE_b/KE_p increased. In Fig. 7, the D_b/D_p yielding maximum lateral displacement shifts similarly from 2–4 to 4 as KE_b/KE_p increases from 1/128 to 1/8. This similarity explains the high correlation of the magnitude of the lateral displacement of the penetrator to the depth of penetration. The critical D_b/D_p for the minimum P/P_o and maximum lateral displacement does not coincide exactly because the synergistic influence arising from the characteristic shape, erosion, breakage, and lateral displacement of the residual penetrator, etc., is not accounted for in Fig. 7. When minimum P/P_o is achieved ($KE_b/KE_p = 1/8$ and $D_b/D_p = 4$), $\sim 5\%$ of the maximum lateral displacement with reference to the longitudinal flight distance of $4L_p$ is observed.

4 Conclusion

Protection performance of a flying cross bar, instead of flying plate, to incapacitate the long-rod penetrator, has been evaluated numerically. The length to diameter ratio, L/D, of the penetrator was 30 and the velocity was 2.0 km/s. The length of bar was fixed to $0.5L$ and the velocity of the bar was determined from its mass and given kinetic energy. The bar was assumed to impact the mid point of the penetrator at 45 degree of obliquity. The kinetic energy of flying cross bar considered were 1/128–1/8 times KE_p. For each kinetic energy, the diameter of cross bar considered were 0.5–16 times the diameter of the penetrator, D_p. The distances between penetrator and witness block were $2L$–$4L$.

As D_b/D_p increases, P/P_o initially decreases rapidly, but increases back after a minimum P/P_o. The D_b/D_p yielding minimum P/P_o generally shifts from 1.5 to 4.0 as the kinetic energy of the bar KE_b/KE_p increases. Interestingly, as the kinetic energy of the bar KE_b/KE_p grows larger, a relatively wider range of D_b/D_p shows the smaller depth of penetration. As for the influence of G, the overall trend of P/P_o in terms of D_b/D_p for varying KE_b/KE_p is maintained in similar fashion. However, the P/P_o decreases with G significantly at a given condition since the penetrator deforms more with the longer flying time after it is disturbed.

Within the limitations of the current simulation, including the incapability of replicating tensile fracture with crack propagation, simple material models, and assumption of the hitting the midpoint of the penetrator, etc., it was shown that the protection performance of the cross bar could be more efficient than the flying plate, but further rigorous works are necessary to draw out a generalized conclusion on this issue. The magnitude of the lateral displacement of the penetrator is qualitatively well correlated to the resultant depth of penetration in the witness block; other mechanisms such as erosion and breakage of the penetrator are also associated.

Acknowledgments This work was financially supported by Basic Science Research Program through the National Research Foundation of Korea (NRF), funded by the MEST (2010-0004150).

References

1. Liden E, Johansson B, Lundberg B (2006) Effect of thin oblique moving plates on long rod projectiles: A reverse impact study. Int J Impact Eng 32:1696–1720
2. Shin H, Yoo Y-H (2003) Effect of the velocity of a single flying plate on the protection capability against obliquely impacting long rod penetrators. Combust Explos Shock Waves 39:591–600
3. Yoo Y-H, Shin H (2004) Protection capability of dual flying plates against obliquely impacting long rod penetrators. Int J Impact Eng 30:55–68
4. Paik SH, Kim S-J, Yoo Y-H, Lee M (2007) Protection performance of dual flying oblique plate against yawed long rod. Int J Impact Eng 34:1413–1422
5. McIntosh G, Szymczak M (2002) Ballistic protection possibilities for a light armoured vehicle. In: Proceedings of the 20th international symposium on ballistics, Orlando, FL, USA, pp 23-27
6. Sterzelmeier K, Brommer V, Sinninger L (2001) Active armor protection—concept and design of steerable launcher systems fed by modular pulsed-power supply units. IEEE Trans Magnetics 37:238–241
7. Lee W, Lee H-J, Shin H (2002) Ricochet of a tungsten heavy alloy long-rod projectile from deformable steel plates. J Phys D Appl Phys 35:2676–2686

8. Shin H, Lee W (2003) Interactions of impact shock waves in a thin-walled explosive container, part I: impacts by a flat-ended projectile. Combust Explos Shock Waves 39:470–478
9. Shin H, Lee W (2003) Interactions of impact shock waves in a thin-walled explosive container, part II: impact by a cone-nosed projectile. Combust Explos Shock Waves 39:479–486
10. Shin H, Lee W (2003) Material design guidelines for explosive confinements to control impact shock-induced detonations based on shock transmission/reflection analysis. Int J Impact Eng 8:465–478
11. Liden E, Andersson O, Tjernberg A (2007) Influence of side-impacting dynamic armour components on long rod projectiles. In: Proceedings of the 23rd international symposium on ballistics, Tarragona, Spain, pp 16–20
12. Johnson GR, Cook WH (1983) A constitutive model and data for metals subjected to large strains, high strain rated, and high temperatures. In: Proceedings of the 17th international symposium on ballistics, Hague, Netherlands, pp 541–47
13. Liden E, Ottosson J, Holmberg L (1996) WHA long rods penetrating stationary and moving oblique steel plates. In: Proceedings of the 16th international symposium on ballistics, San Francisco, CA, USA, pp 703–11
14. Hallquist JO (2006) LS-DYNA Theory Manual. Livermore Software Technology Corporation, Livermore
15. Anderson CE Jr, Walker JD, Parton SJ, Bless Y (1996) On the *L/D* effect for long-rod penetrators. Int J Impact Eng 18:247–264
16. Anderson CE Jr, Walker JD, Bless SJ, Sharron TR (1995) On the velocity dependence of the *L/D* effect for long-rod penetrators. Int J Impact Eng 17:13–24